Check for updates

ADVANCED MATERIALS
www.advmat.de

Enhanced Hydrogen Evolution Reaction in Alkaline Media via Ruthenium–Chromium Atomic Pairs Modified Ruthenium Nanoparticles

Parisa Eskandari, Shujie Zhou, Jodie Yuwono, Denny Gunawan, Richard F. Webster, Zhipeng Ma, Hanyu Xu, Rose Amal, and Xunyu Lu**

Precisely optimizing the electronic metal support interaction (EMSI) of the electrocatalysts and tuning the electronic structures of active sites are crucial for accelerating water adsorption and dissociation kinetics in alkaline hydrogen evolution reaction (HER). Herein, an effective strategy is applied to modify the electronic structure of Ru nanoparticles (Ru_{NPs}) by incorporating Ru single atoms (Ru_{SAs}) and Ru and Cr atomic pairs ($RuCr_{APs}$) onto a nitrogen-doped carbon (N–C) support through optimized EMSI. The resulting catalyst, Ru_{NPs}-$RuCr_{APs}$-N-C, shows exceptional performance for alkaline HER, achieving a six times higher turnover frequency (TOF) of 13.15 s^{-1} at an overpotential of 100 mV, compared to that of commercial Pt/C (2.07 s^{-1}). Additionally, the catalyst operates at a lower overpotential at a current density of 10 mA·cm^{-2} (η_{10} = 31 mV), outperforming commercial Pt/C (η_{10} = 34 mV). Experimental results confirm that the $RuCr_{APs}$ modified Ru_{NPs} are the main active sites for the alkaline HER, facilitating the rate-determining steps of water adsorption and dissociation. Moreover, the Ru–Cr interaction also plays a vital role in modulating hydrogen desorption. This study presents a synergistic approach by rationally combining single atoms, atomic pairs, and nanoparticles with optimized EMSI effects to advance the development of efficient electrocatalysts for alkaline HER.

1. Introduction

Electrocatalytic water splitting processes using renewable electricity sources are recognized as effective and sustainable strategies to produce green hydrogen, effectively addressing the issue of unbalanced energy distribution.[1] Alkaline water electrolysis has advantages over its acidic counterpart due to its greater stability, higher feasibility in practical operation, and cost-effectiveness.[2] However, alkaline hydrogen evolution reaction (HER) suffers from slow kinetic rates and low activity due to additional water adsorption and dissociation steps, which require more energy, thus hindering affordable and scalable hydrogen production.[3] Therefore, it is critical to develop efficient electrocatalysts with optimized water adsorption and dissociation abilities.

Ruthenium (Ru), known for its strong affinity for the hydroxyl intermediate (OH*), has a high potential to enhance the water dissociation reaction rate and hence has been reported to exhibit higher HER activity than the benchmark platinum (Pt) in alkaline media.[4] Furthermore, the unit cost of Ru is ≈4% that of Pt, making Ru more affordable for large-scale applications.[5] However, the severe aggregation of Ru atoms because of high surface energy has limited the atom utilization. Moreover, Ru exhibits excessively strong adsorption to hydrogen intermediates (H*), which hampers the desorption of H* from the surface.[6] Considering these challenges, it is crucial to develop strategies to achieve low-loading Ru-based catalysts with optimized water adsorption, and dissociation, and hydrogen desorption capabilities.

P. Eskandari, S. Zhou, D. Gunawan, Z. Ma, H. Xu, R. Amal, X. Lu
School of Chemical Engineering
University of New South Wales (UNSW) Sydney
Kensington, NSW 2052, Australia
E-mail: shujie.zhou@unsw.edu.au; xunyu.lu@unsw.edu.au

The ORCID identification number(s) for the author(s) of this article can be found under https://doi.org/10.1002/adma.202419360

© 2025 The Author(s). Advanced Materials published by Wiley-VCH GmbH. This is an open access article under the terms of the Creative Commons Attribution-NonCommercial-NoDerivs License, which permits use and distribution in any medium, provided the original work is properly cited, the use is non-commercial and no modifications or adaptations are made.

DOI: 10.1002/adma.202419360

J. Yuwono
School of Chemical Engineering
University of Adelaide
Adelaide, South Australia 5005, Australia

R. F. Webster
Electron Microscope Unit
Mark Wainwright Analytical Centre
UNSW
Sydney, NSW 2052, Australia

R. F. Webster
School of Materials Science and Engineering
UNSW
Sydney, NSW 2052, Australia

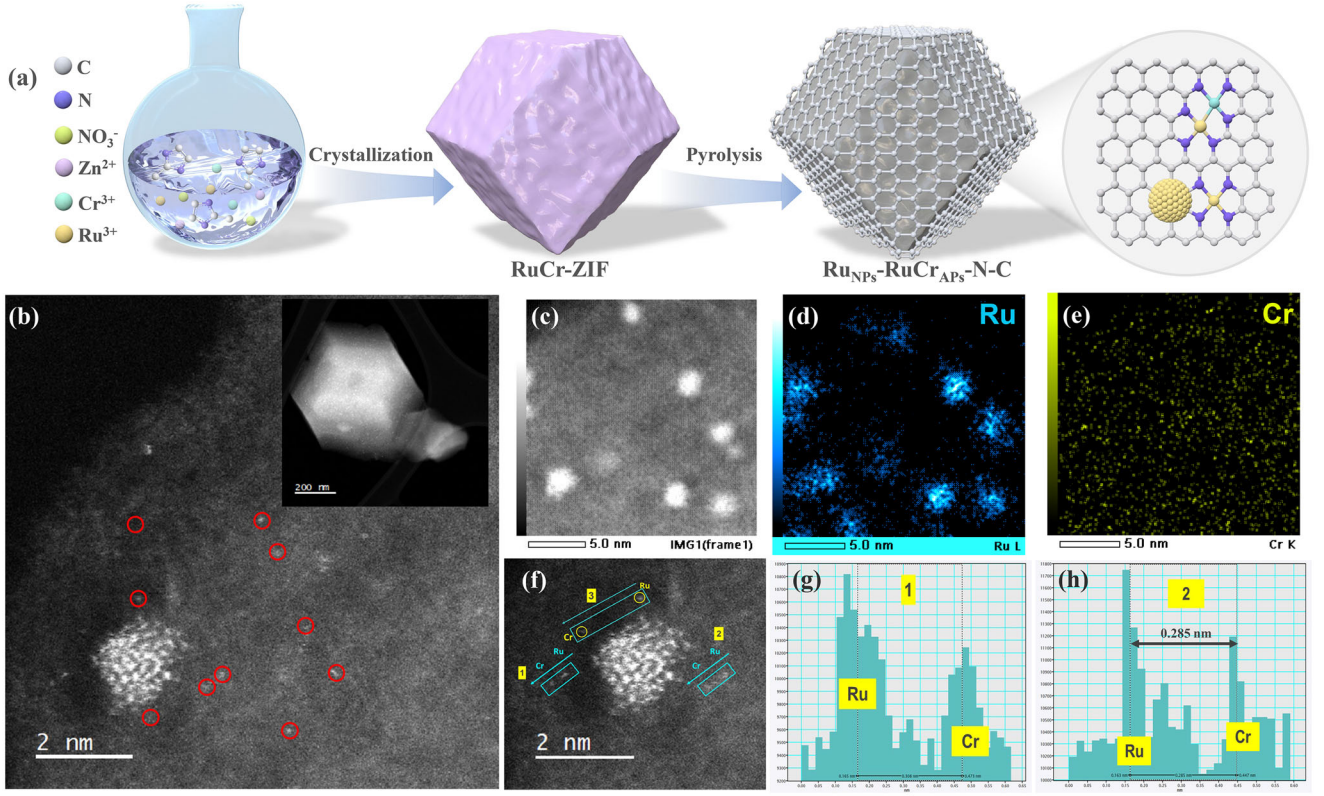

Figure 1. a) Schematic of the synthesis method of Ru_{NPs}-$RuCr_{APs}$-N-C, b) Aberration corrected HAADF-STEM image (inset: ZIF-8 structure, Ru and Cr atoms were marked with red circles), c–e) EDS mapping images, and f–h) Intensity profiles of Ru_{NPs}-$RuCr_{APs}$-N-C (1,2 linear profile scan of different regions of the catalyst).

Recent studies have shown that incorporating both Ru single atoms (SAs) and nanoparticles (NPs) onto a support is a promising strategy to enhance the water dissociation rate, improve HER activity, and at the same time maximize the Ru utilization.[7] For example, Hu et al. showed that the co-existence of Ru SAs, which have a low water dissociation barrier, alongside Ru NPs that exhibit optimal hydrogen adsorption and desorption properties, is beneficial for enhancing alkaline HER performance.[8] Wang's group showed that Ru NPs enhance the water dissociation to generate adsorbed hydrogen, while Ru SAs (Ru–N_4 sites) combine the adsorbed hydrogen into H_2 and facilitate its desorption. Therefore, the synergistic interaction between Ru NPs and SAs modifies the electronic structure, accelerating the overall HER kinetics.[9] The study by Yao's group also confirmed that the strong electronic coupling effects between Ru NPs and SAs accelerate water dissociation and optimize the bond strength of H* leading to improved HER activity.[10] While Ru SAs have been shown to modify Ru NPs and enhance HER activity, the HER performance still needs to be further improved. Besides, the impact of Ru SAs on the electrocatalytic behavior of supported metal NPs, particularly through electronic metal support interactions (EMSI), remains largely unexplored. The EMSI plays an important role in modifying the activity of the catalysts by tuning the electron distribution and regulating the water adsorption and dissociation ability.[11] In this regard, precisely introducing a second metal single atom is considered a promising strategy to further tune the EMSI effects and modify the catalytic properties of Ru NPs. However, it is of great importance yet challenging to understand the specific roles and interaction between the second metal atoms, NPs, and SAs through EMSI.

In this study, we investigate the impact of introducing a second atomic species with the presence of atomic pairs and dual SAs to optimize EMSI effects and modify the properties of Ru NPs. To achieve this, we prepared a composite catalyst (Ru_{NPs}-$RuCr_{APs}$-N-C) consisting of Ru_{NPs}, Ru_{SAs}, $Cr_{SAs,}$ and RuCr atomic pairs ($RuCr_{APs}$) dispersed on the nitrogen-doped carbon (N-C). Combining the experimental and the theoretical studies, the roles of different species, NPs, SAs, and APs, in the catalysts are identified. It is found that electronically $RuCr_{APs}$ modified Ru NPs are proven as active sites with high electron-enriched environment for alkaline HER, which exhibit higher water adsorption and dissociation ability compared to bare Ru NPs catalyst (Ru_{NPs}-N-C) as a result of optimized EMSI effects. Moreover, the Ru atoms from the $RuCr_{APs}$ are confirmed to be more beneficial for hydrogen desorption.

2. Results and Discussion

2.1. Catalyst Preparation and Characterization

The procedure of synthesis and preparation of Ru_{NPs}-$RuCr_{APs}$-N-C is illustrated in **Figure 1a** with details provided in the experimental section in Supporting Information. During the crystallization of ZIF-8 (average size d = 50 nm), ruthenium

© 2025 The Author(s). Advanced Materials published by Wiley-VCH GmbH

15214095, 2025, 34, Downloaded from https://advanced.onlinelibrary.wiley.com/doi/10.1002/adma.202419360 by University of Adelaide Alumni, Wiley Online Library on [02/11/2025]. See the Terms and Conditions (https://onlinelibrary.wiley.com/terms-and-conditions) on Wiley Online Library for rules of use; OA articles are governed by the applicable Creative Commons License

15214095, 2025, 34, Downloaded from https://advanced.onlinelibrary.wiley.com/doi/10.1002/adma.202419360 by University of Adelaide Alumni, Wiley Online Library on [02/11/2025]. See the Terms and Conditions (https://onlinelibrary.wiley.com/terms-and-conditions) on Wiley Online Library for rules of use; OA articles are governed by the applicable Creative Commons License

acetylacetonate ($Ru(acac)_3$) and chromium nitrate nonahydrate ($Cr(NO_3)_3{\cdot}9H_2O$) were added, and silica (SiO_2) was used as a template to increase the surface area of the formed ZIF-8. The distinctive structure of ZIF-8 enables the formation of neighboring metal dimers through the following mechanisms: 1) in situ encapsulation of cage-separated metal precursors, 2) utilization of nitrogen species derived from organic templates to facilitate metal-N coordination within the carbon skeleton, and 3) evaporation of low boiling-point zinc nodes during calcination, ensuring the isolated distribution of dimeric metal sites.[12] The size of $Ru(acac)_3$ is 9.8 Å, which is between the size of the central cavities (d = 11.6 Å) and the apertures (d = 3.4 Å) of ZIF-8.[13] This facilitates the incorporation of Ru into the cavities of the newly formed ZIFs during the process. The sample was pyrolyzed at 950 °C in an Ar atmosphere to evaporate Zn, followed by the removal of SiO_2 in a NaOH solution. After the second calcination, the catalysts were obtained. The catalysts contain only Ru NPs (Ru_{NPs}-N-C), a mixture of Ru NPs and SAs (Ru_{NPs}-Ru_{SAs}-N-C) and only Cr SAs (Cr_{SAs}-N-C) were also prepared following the same procedure as stated in the supporting information. The optimal amounts of $Ru(acac)_3$ and Cr $(NO_3)_3{\cdot}9H_2O$ were also determined to be 0.15 and 0.025 mmol respectively, (see supporting information) based on X-ray diffraction (XRD) patterns (Figures S1 and S4, Supporting Information), HER activity (Figures S2 and S5, Supporting Information) and electrochemical surface area (ECSA, Figure S3, Supporting Information). Moreover, different RuM-N-C (M: Co, Ni, Cu, Mo, and Mn) catalysts following the similar preparation method of Ru_{NPs}-$RuCr_{APs}$-N-C catalyst have been synthesized and tested. Comparison the HER activity of these catalysts (Figure S6, Supporting Information) shows that Ru_{NPs}-$RuCr_{APs}$-N-C exhibits the best HER performance.

The structure and morphology of the catalyst were investigated using different characterization techniques. The powder XRD patterns of the Ru_{NPs}-Ru_{SAs}-N-C, Ru_{NPs}-$RuCr_{APs}$-N-C, and Cr_{SAs}-N-C samples (Figure S4, Supporting Information) exhibit characteristic broad peaks at ≈25 and 43°, corresponding to the (002) and (101) planes of graphitic carbon, respectively.[14] There are no peaks associated with Ru and Cr metal nanoparticles, suggesting the absence of nanoparticles or that their low contents are beyond the detection limit. The loading of Ru and Cr is found to be 1.28 and 0.08 wt.% for Ru_{NPs}-$RuCr_{APs}$-N-C respectively by inductively coupled plasma–mass spectrometry (ICP-MS) analysis. Meanwhile, the Ru content in Ru_{NPs}-Ru_{SAs}-N-C is determined to be 1.15 wt.%, closely matching that of Ru_{NPs}-$RuCr_{APs}$-N-C. Raman spectroscopy was used to determine the structural features of the carbon matrix. The Raman spectra of Ru_{NPs}-Ru_{SAs}-N-C and Ru_{NPs}-$RuCr_{APs}$-N-C exhibit two peaks at ≈1350 and 1590 $cm^{-1,}$ corresponding to D and G bands, respectively (Figure S7, Supporting Information).[15] D band reflects defective carbon while the G band corresponds to graphitic carbon.[16] The intensity ratio of D to G (I_D/I_G) is calculated to be 1.2 and 1.01 for Ru_{NPs}-$RuCr_{APs}$-N-C and Ru_{NPs}-Ru_{SAs}-N-C respectively. The incorporation of Cr and the presence of $RuCr_{APs}$ introduce more structural disorder due to the change in the coordination structure of the catalyst. Ru_{NPs}-Ru_{SAs}-N-C exhibits Ru–N_4 coordination, whereas Ru_{NPs}-$RuCr_{APs}$-N-C features N–Ru–Cr–N and extra Cr-N_4 coordination, inducing changes in the carbon matrix. The Raman spectra of Ru_{NPs}-$RuCr_{APs}$-N-C and Ru_{NPs}-Ru_{SAs}-N-C exhibit two peaks at ≈1350 and 1590 cm^{-1} which are D and G bands respectively (Figure S7, Supporting Information).[15a] D band reflects defective carbon and G band corresponds to graphitic carbon.[15a] The change in the coordination structure of the catalysts, leads to more defects and structural disorder and hence higher I_D/I_G ratio of Ru_{NPs}-$RuCr_{APs}$-N-C.[17] Moreover, the morphology of the Ru_{NPs}-$RuCr_{APs}$-N-C and Ru_{NPs}-Ru_{SAs}-N-C was investigated by transmission electron microscopy (TEM). It indicates that the catalysts have a rhombic dodecahedron morphology with the particle size of ≈500 nm, which is a typical of the ZIF-8 structure (Figure 1b inset).[18] The TEM images (Figure S8a,b, Supporting Information) reveal a uniform dispersion of Ru_{NPs} on the support, with an average particle size ranging from 1.5 to 2.5 nm. Furthermore, the corresponding size distribution curve (Figure S8c, Supporting Information) exhibits a narrow particle size distribution, confirming the high uniformity in Ru_{NPs} and the good monodispersity. Furthermore, the high angle annular dark-field scanning transmission electron microscopy (HAADF-STEM) images of Ru_{NPs}-$RuCr_{APs}$-N-C (Figure 1b) and Ru_{NPs}-Ru_{SAs}-N-C (Figure S9a, Supporting Information) reveal the co-existence of nanoparticles and single atoms (marked by red circles) dispersed on the carbon support. Moreover, the energy-dispersive X-ray spectroscopy (EDS) mapping (Figure 1c-e and Figure S8d, Supporting Information) confirms the presence of C, N, Ru and Cr and it indicates that Ru exists as a mixture of NPs, and SAs while Cr is highly likely to be SAs as there is no aggregation. The co-existence of Ru NPs and Ru SAs is also observed in the EDS mapping of Ru_{NPs}-Ru_{SAs}-N-C (Figure S9f, Supporting Information). The distance between the crystal planes of the metal particles is measured to be 0.23 nm, corresponding to the (10-10) plane of hexagonal Ru (Figure S8e, Supporting Information).[19] The intensity in HAADF-STEM is from Rutherford scattering and is proportional to atomic number, Z^2 here, intensity profiles from different regions can be used to identify the species of single atom catalysts.[20] Figure 1f–h and Figure S8f (Supporting Information) show intensity profiles with distinct peak intensities indicating that there are two species of atoms present. In correlation with the EDS which showed the presence of both Ru and Cr in NP free regions, the brighter atoms can be assigned as atomic Ru while those with lower intensities can be assigned as atomic Cr according to their atomic number. The enlarged image of the region highlighted in Figure 1f shows that there are two types of atomic Ru and Cr. The first consists of separately dispersed Ru SAs and Cr SAs (Figure S8f, Supporting Information, linear scan profile of region 3), while the second forms a Ru-Cr diatomic structure ($RuCr_{APs}$) with an average interatomic distance of ≈3.0 Å (Figure 1g and h, linear scan profile of region 1 and 2 in Figure 1f). By comparison, the line profile of Ru_{NPs}-Ru_{SAs}-N-C shows that all of the single atoms have the same HAADF intensity indicating just one atom species, Ru, is present (Figure S9b, Supporting Information).

The structures of Ru_{NPs}-$RuCr_{APs}$-N-C and Ru_{NPs}-Ru_{SAs}-N-C and the coordination states of Ru and Cr were further characterized using synchrotron-based X-ray absorption spectroscopy (XAS). The X-ray absorption near edge structure (XANES), k^3-weighted extended X-ray absorption fine structure (EXAFS), and associated Fourier transform (FT EXAFS) at the Ru K-edge and Cr K-edge are presented in **Figures 2** and S10 (Supporting Information). The XANES data at the Ru K-edge (Figure 2a) reveal the K-edge position of Ru in both Ru_{NPs}-$RuCr_{APs}$-N-C and

© 2025 The Author(s). Advanced Materials published by Wiley-VCH GmbH

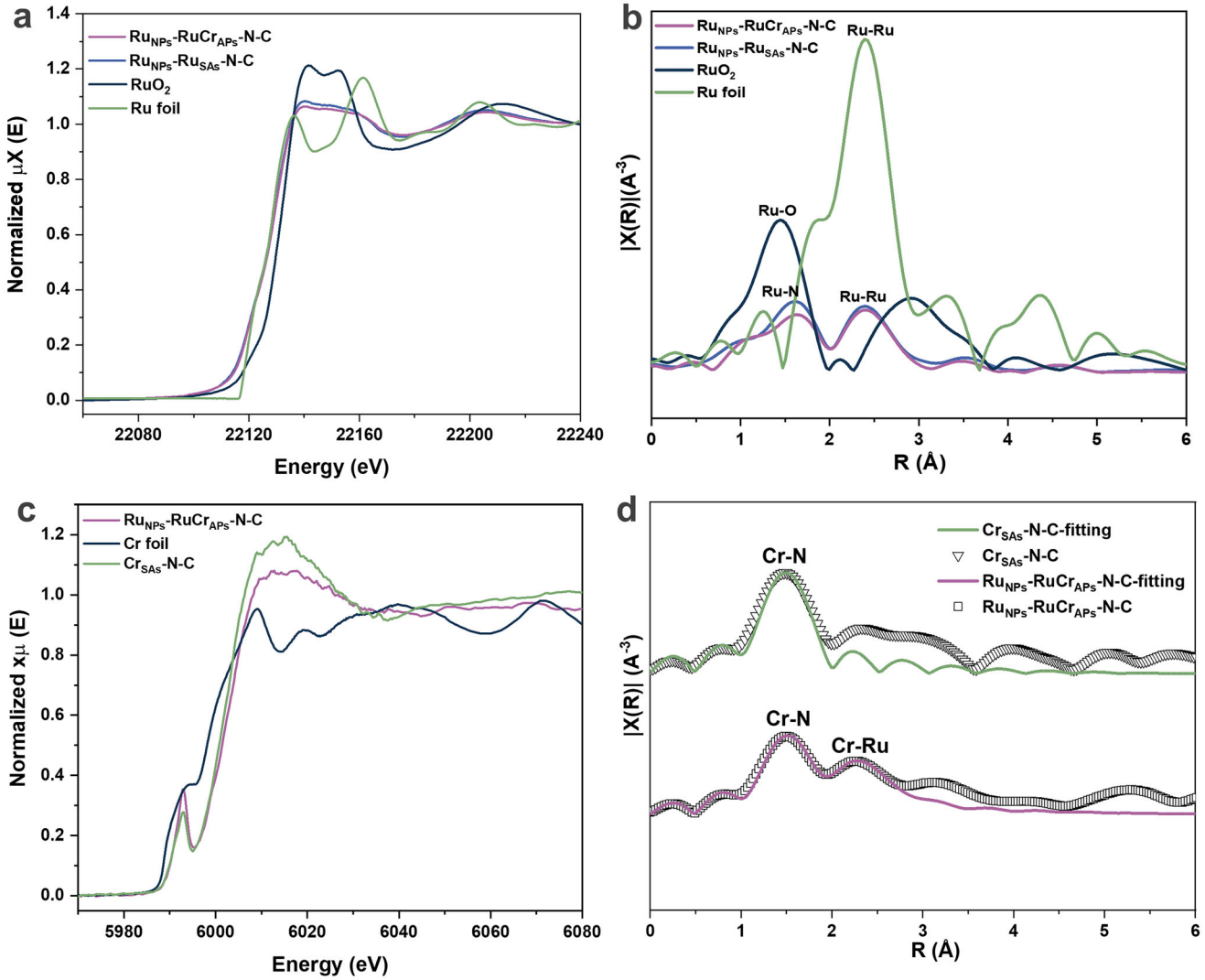

Figure 2. a) XANES of Ru$_{NPs}$-Ru$_{SAs}$-N-C, Ru$_{NPs}$-RuCr$_{APs}$-N-C, Ru foil and RuO$_2$ at Ru K-edge, b) Fourier transform of the $k^3\chi(k)$ EXAFS of Ru$_{NPs}$-Ru$_{SAs}$-N-C, Ru$_{NPs}$-RuCr$_{APs}$-N-C, Ru foil and RuO$_2$ at Ru K-edge, c) XANES of Cr$_{SAs}$-N-C, Ru$_{NPs}$-RuCr$_{APs}$-N-C, and Cr foil at Cr K-edge, and d) Fit of the Fourier transform of the $k^3\chi(k)$ EXAFS of Cr$_{SAs}$-N-C and Ru$_{NPs}$-RuCr$_{APs}$-N-C at Cr K-edge.

Ru$_{NPs}$-Ru$_{SAs}$-N-C is slightly higher compared to that of Ru foil, suggesting that the average valence state of Ru in these structures is greater than zero. Furthermore, the Ru K-edge FT EXAFS data (Figure 2b) confirm the presence of Ru-Ru and also Ru-N peaks in both Ru$_{NPs}$-RuCr$_{APs}$-N-C and Ru$_{NPs}$-Ru$_{SAs}$-N-C, indicating the existence of Ru nanoparticles (NPs). These findings align with the TEM results, which also confirmed the presence of Ru NPs. Based on the fittings in Figure S10b (Supporting Information), both Ru$_{NPs}$-RuCr$_{APs}$-N-C and Ru$_{NPs}$-Ru$_{SAs}$-N-C exhibit a similar Ru-Ru coordination number and bond length of 2.3 ± 0.6 and 2.69 Å,[21] respectively. This suggests no change in coordination number and the bond length of Ru NPs in Ru$_{NPs}$-RuCr$_{APs}$-N-C by introducing Cr SAs. The Ru–Ru bond length in the Ru NPs of both Ru$_{NPs}$-RuCr$_{APs}$-N-C and Ru$_{NPs}$-Ru$_{SAs}$-N-C is slightly longer compared to that in Ru foil, which can be attributed to the smaller size of the nanoparticles.[22] In addition, the Ru K-edge FT EXAFS data show the presence of Ru-N peaks. The fitting for Ru$_{NPs}$-Ru$_{SAs}$-N-C catalyst shows that the Ru-N bond has a coordination number of 3.4 ± 0.6 and a bond length of 2.02 Å,[23] suggesting the formation of Ru-N$_4$ in the structure. On the other hand, the fitting of Ru$_{NPs}$-RuCr$_{APs}$-N-C also confirms the existence of Ru–N bond with the coordination number of 2.7 ± 0.6 and bond length of 2.01 Å.[24] The changes in the coordination number and the bond length indicate that introducing Cr can change the electronic structure of Ru SAs in Ru$_{NPs}$-RuCr$_{APs}$-N-C catalyst. Moreover, the FT EXAFS and the fitting of Cr K-edge (Figure 2d) show that there are no Cr NPs in Cr$_{SAs}$-N-C and Ru$_{NPs}$-RuCr$_{APs}$-N-C and hence Cr is single atoms. The presence of a Cr-N peak corresponding to the Cr-N$_4$ structure (Cr-N bond length of 1.99 Å) in Cr$_{SAs}$-N-C confirms the structural consistency and coordination environment of Cr single atoms within the catalyst. In addition, there are two peaks observed from the fitting results of Ru$_{NPs}$-RuCr$_{APs}$-N-C, which show that Cr is coordinated to N (1.95 Å) and Ru$_{SAs}$ (2.54 Å), with the plausible structure of Cr-N$_4$ and

© 2025 The Author(s). Advanced Materials published by Wiley-VCH GmbH

15214095, 2025, 34, Downloaded from https://advanced.onlinelibrary.wiley.com/doi/10.1002/adma.202419360 by University of Adelaide Alumni, Wiley Online Library on [02/11/2025]. See the Terms and Conditions (https://onlinelibrary.wiley.com/terms-and-conditions) on Wiley Online Library for rules of use; OA articles are governed by the applicable Creative Commons License

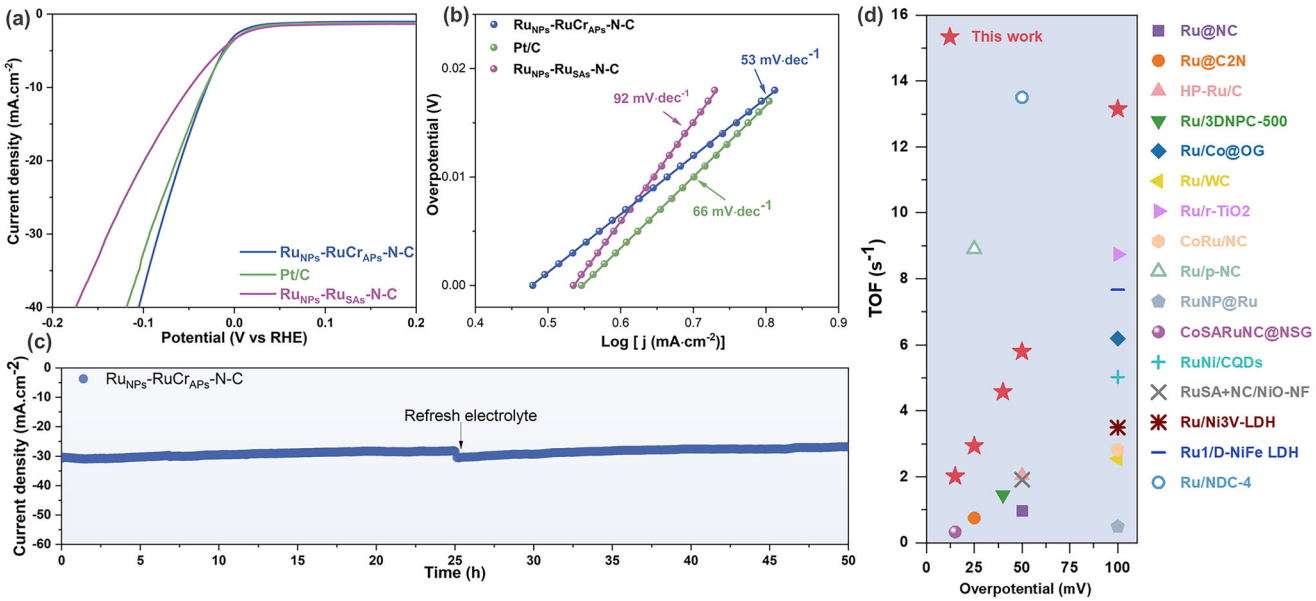

Figure 3. a) Polarization curves at a scan rate of 5 mV s^{-1}, b) Tafel plots, c) stability curves of Ru_{NPs}-$RuCr_{APs}$-N-C, and d) TOF comparison of Ru_{NPs}-$RuCr_{APs}$-N-C with other Ru-based electrocatalysts[22,29] and the detailed information is provided in Table S3, Supporting Information).

N-Ru-Cr-N respectively. Considering the change in the coordination number and the interaction between atomic Ru and Cr, it can be concluded that in the Ru_{NPs}-Ru_{SAs}-N-C catalyst the structure of Ru SAs is Ru-N_4, while there are two types of atomic Ru in Ru_{NPs}-$RuCr_{APs}$-N-C, including Ru-N_4 and N-Ru-Cr-N. Therefore, the XAS results confirm the Ru_{NPs}-$RuCr_{APs}$-N-C catalyst consists of the mixture of Ru NPs, Ru SAs and Cr SAs, with the presence of RuCr atomic pairs (Ru-Cr bond length of 2.54 Å), which are in good agreement with the aberration-corrected STEM results (Ru-Cr bond length of ≈3 Å). Additionally, to further understand the chemical states of Ru and Cr and the effect of RuCr atomic interaction on the electronic structure of the Ru NPs, X-ray photoelectron spectroscopy (XPS) was performed (Figure S11, Supporting Information). The XPS spectra of Ru_{NPs}-$RuCr_{APs}$-N-C confirm the presence of C, N, and Ru while the signals corresponding to Cr 2p are not detected, due to its low concentration and the detection limits of XPS instrument (Figure S11a, Supporting Information). The XPS analysis show that Ru 3p spectra of Ru_{NPs}-$RuCr_{APs}$-N-C (Figure S11b, Supporting Information) shift to lower binding energy compared to Ru_{NPs}-Ru_{SAs}-N-C, indicating the lowered oxidation states of Ru in the Ru_{NPs}-$RuCr_{APs}$-N-C composite due to the formation of RuCr atomic pairs. This indicates the electron redistribution due to the presence of RuCr atomic pairs with increased electron density in Ru_{NPs}-$RuCr_{APs}$-N-C through EMSI effects, which is beneficial for water adsorption and dissociation ability in alkaline HER.[25] The XPS results are in good agreement with Ru K-edge XANES spectra of Ru_{NPs}-$RuCr_{APs}$-N-C (Figure 2a) which also show lower white line intensity compared to that of Ru_{NPs}-Ru_{SAs}-N-C, indicating lower oxidation states and more electron-enriched environments of Ru NPs sites in Ru_{NPs}-$RuCr_{APs}$-N-C. Besides, the Cr K-edge XANES spectra in Figure 2c for Ru_{NPs}-$RuCr_{APs}$-N-C show a positive shift compared to that of Cr_{SAs}-N-C, suggesting a reduced electron density on Cr sites. This indicates that the Cr in the $RuCr_{APs}$ donates the electrons to Ru sites, enabling the electron redistribution in the Ru_{NPs}-$RuCr_{APs}$-N-C and a modified EMSI.

2.2. Electrocatalytic Performance for HER

The alkaline HER activity of Ru_{NPs}-$RuCr_{APs}$-N-C was compared with that of Ru_{NPs}-Ru_{SAs}-N-C and commercial Pt/C. As displayed in **Figure** 3a, Ru_{NPs}-$RuCr_{APs}$-N-C exhibit highest activity with a near-zero onset potential. The overpotential required to reach the current density of 10 mA cm^{-2} (η_{10}) is decreased to merely 31 mV for Ru_{NPs}-$RuCr_{APs}$-N-C, representing a significant catalytic improvement compared to 87 mV for Ru_{NPs}-Ru_{SAs}-N-C, and even better than the commercial Pt/C catalyst containing 20 wt% Pt (η_{10} = 34 mV). Moreover, the HER kinetics of the catalyst were examined through Tafel analysis. The results (Figure 3b) indicate that Ru_{NPs}-$RuCr_{APs}$-N-C has the lowest Tafel slope of 53 mV·dec^{-1}, outperforming both 20% Pt/C (66 mV.dec^{-1}) and Ru_{NPs}-Ru_{SAs}-N-C (92 mV.dec^{-1}), suggesting the fastest kinetic rate. The lower Tafel slope is consistent with the HER activity results, confirming the crucial role of Cr SAs and the interaction of RuCr atomic pairs in enhancing the reaction kinetics. Additionally, electrochemical impedance spectroscopy (EIS) measurements were conducted to study the solid-electrolyte interfacial properties and charge transfer resistance. The fitted EIS data reveals a semicircular shape in which the diameter of these semicircles indicates the charge transfer kinetic of the electrocatalysts.[26] The Fitting results are shown in Figure S12 and Table S1 (Supporting Information). R_1 represents the electrolyte resistance while R_2 is attributed to the internal resistance of the electrode. R_3 corresponds to the charge transfer resistance (R_{CT}) at the catalyst-electrolyte interface, governing the kinetics of electron transfer processes essential for catalytic activity.[27] In this study, R_1 and R_2 values for both Ru_{NPs}-Ru_{SAs}-N-C and Ru_{NPs}-$RuCr_{APs}$-N-C are similar due to the identical electrolyte composition and using the

© 2025 The Author(s). Advanced Materials published by Wiley-VCH GmbH

15214095, 2025, 34, Downloaded from https://advanced.onlinelibrary.wiley.com/doi/10.1002/adma.202419360 by University of Adelaide Alumni, Wiley Online Library on [02/11/2025]. See the Terms and Conditions (https://onlinelibrary.wiley.com/terms-and-conditions) on Wiley Online Library for rules of use; OA articles are governed by the applicable Creative Commons License

same electrode in a three-electrode system. However, the fitting results demonstrate that Ru_{NPs}-$RuCr_{APs}$-N-C exhibits the smallest semicircle of the Nyquist plots (Figure S12, Table S1, Supporting Information) and the fastest charge transfer kinetics with R_3 value of 38.83 Ω (Figure S12 inset, Table S1, Supporting Information) compared to that of Ru_{NPs}-Ru_{SAs}-N-C (73.41 Ω). This implies significantly reduced charge transfer resistance, indicative of enhanced electron transfer kinetics at the Ru–electrolyte interface for Ru_{NPs}-$RuCr_{APs}$-N-C due to the presence of RuCr atomic pairs, which optimize EMSI and contributes to the improved HER activity shown in Fig 3a. Besides, the electrochemical surface area (ECSA) of these catalysts was measured based on copper (Cu) underpotential deposition (Cu-UPD) method (Figure S13, Supporting Information).[28] The ECSA of Ru_{NPs}-$RuCr_{APs}$-N-C is calculated to be 205.07 $m^2 \cdot g^{-1}$, implying its abundant active sites. The mass activity and the specific activity of Ru_{NPs}-$RuCr_{APs}$-N-C were also measured (Figure S14, Supporting Information). It can be seen that the specific activities follow a set order of Ru_{NPs}-$RuCr_{APs}$-N-C > Ru_{NPs}-Ru_{SAs}-N-C > Pt/C. The ECSA normalized current density of Ru_{NPs}-$RuCr_{APs}$-N-C obtains 5.52 $mA \cdot cm^{-2}$ at the overpotential of 100 mV, ≈3 times higher compared to that of Ru_{NPs}-Ru_{SAs}-N-C(2.06 $mA \cdot cm^{-2}$), and over six times higher than that of commercial Pt/C (0.87 $mA \cdot cm^{-2}$). Similarly, the mass activity of Ru_{NPs}-$RuCr_{APs}$-N-C (11.33 $A \cdot mg^{-1}$) at an overpotential of 100 mV is found to be ≈2 times and 18 times higher than those of Ru_{NPs}-Ru_{SAs}-N-C (6.11 $A \cdot mg^{-1}$) and 20% Pt/C (0.63 $A \cdot mg^{-1}$), respectively. Furthermore, a comparison with recent Ru-based electrocatalysts (Table S2, Supporting Information) highlights the remarkably high mass activity of Ru_{NPs}-$RuCr_{APs}$-N-C, which is comparable to or even superior to the state-of-the-art catalysts. Moreover, the turnover frequency (TOF) is employed to represent the intrinsic activity of a catalyst. The TOF of Ru_{NPs}-$RuCr_{APs}$-N-C is 13.15 s^{-1} at an overpotential of 100 mV, indicating its high intrinsic activity, which is ≈3 times and six times higher than the TOF of Ru_{NPs}-Ru_{SAs}-N-C (5.06 s^{-1}) and commercial Pt/C (2.07 s^{-1}), respectively. It also outperforms most of the reported Ru-based electrocatalysts up to date (Figure 3d and Table S3, Supporting Information). In addition to demonstrating exceptional activity and high reaction kinetics, Ru_{NPs}-$RuCr_{APs}$-N-C shows remarkable stability under an alkaline solution during 50 h with negligible change in current density (Figure 3c, after 25 h the fresh electrolyte was used) and no changes in activity (Figure S15, Supporting Information). By contrast, Ru_{NPs}-Ru_{SAs}-N-C and Pt/C exhibit noticeable degradation of 64% and 27% in current density over 25 h (Figure S16, Supporting Information), respectively, implying the instability of these two catalysts. These results highlight the promising HER performance of Ru_{NPs}-$RuCr_{APs}$-N-C in alkaline solutions and suggest the pivotal role of atomic Cr along with the interaction of RuCr atomic pairs in modulating the EMSI effects and improving the catalytic properties of active sites. This ultimately contributes to the improved HER performance and stability of Ru-based catalysts.

2.3. Understanding the Role of Ru and Cr

To elucidate the HER electrocatalytic mechanism, it is necessary to identify the main active sites in the Ru_{NPs}-$RuCr_{APs}$-N-C catalyst. There are four possible active sites within the catalyst: Ru NPs, Ru SAs, Cr SAs, and $RuCr_{APs}$. **Figure 4a** compares the HER electrocatalytic activity of Cr_{SAs}-N-C, Ru_{NPs}-N-C, Ru_{NPs}-Ru_{SAs}-N-C and Ru_{NPs}-$RuCr_{APs}$-N-C. As it can be seen, the HER activity of Cr_{SAs}-N-C is negligible, confirming that bare Cr SAs are not active for HER. Meanwhile, the performance of the catalyst with the co-existence of Ru NPs and Ru SAs (Ru_{NPs}-Ru_{SAs}-N-C) is higher than that of Ru_{NPs}-N-C, indicating enhancement effects are caused by the Ru SAs and tuned EMSI effects. Furthermore, the superior activity of Ru_{NPs}-$RuCr_{APs}$-N-C compared to that of Ru_{NPs}-Ru_{SAs}-N-C suggests that the presence of RuCr atomic pairs further contributes to the activity. To further elucidate the roles of Ru SAs, RuCr atomic pairs and Ru NPs in catalysing the HER, a series of poisoning experiments were conducted using ethylenediaminetetraacetic acid (EDTA) and potassium thiocyanate (KSCN) as poisoning agents. EDTA is known to primarily form coordination bonds with Ru–N/C interfacial sites, while KSCN is adsorbed onto both the Ru surface and Ru–N/C sites (Figure 4b inset).[29i,30] Therefore, EDTA can inhibit the activity of Ru SAs while KSCN has the capability to deactivate all Ru species. As shown in Figure 4b and Figure S17a (Supporting Information), after adding 10 mM EDTA into 1 M KOH solution, the HER activity of the Ru_{NPs}-$RuCr_{APs}$-N-C catalyst experiences negligible changes while it decreases significantly after the addition of 10 mM KSCN. To be specific, the onset and the η_{10} of the Ru_{NPs}-$RuCr_{APs}$-N-C increases from 10 and 31 mV in KOH solution to 81 and 200 mV when adding KSCN to KOH solution, respectively. This observation reveals that the Ru NPs are the main active sites for the HER while the Ru SAs and RuCr atomic pairs play supporting roles. To further distinguish the roles of Ru NPs and the Ru SAs played during the HER catalysis, a catalyst with only Ru and Cr SAs (denoted as $Ru_{SAs}Cr_{SAs}$-N-C) was prepared and its HER performance is shown in Figure S17b (Supporting Information). The η_{10} of $Ru_{SAs}Cr_{SAs}$-N-C is 130 mV, which is higher than that of the Ru_{NPs}-$RuCr_{APs}$-N-C (31 mV Figure S17b, Supporting Information). This further confirms that the main HER-active centres in the Ru_{NPs}-$RuCr_{APs}$-N-C electrocatalyst are the modified Ru NPs. Besides, it is confirmed that the formation of RuCr atomic pairs is essential for optimizing the EMSI effects and enhancing the HER performance, as the physically mixed Ru_{NPs}-Ru_{SAs}-N-C and Cr_{SAs}-N-C composite (physically mixture Ru_{NPs}-Ru_{SAs}-N-C + Cr_{SAs}-N-C) shows much lower HER activity compared with that of Ru_{NPs}-$RuCr_{APs}$-N-C (Figure S17b, Supporting Information).

2.4. Unravelling the HER Mechanisms of the Electrocatalysts

Alkaline HER is commonly considered to occur through a multistep electrochemical mechanism, in which the electrode surface participates via electrocatalytic adsorption and desorption processes. There are two steps for alkaline HER: the first is the Volmer step, where water is adsorbed and reduced to form *H-adsorbed intermediates (where the asterisks denote surface-adsorbed species) (Equation 1). The second step involves the conversion of H* to H_2, which can occur through two pathways: the Heyrovsky step (Equation 2), where electrochemical recombination happens between H* and H_2O, or the Tafel step (Equation 3), where chemical recombination takes place between two H*.[4a,31] The Tafel slope is a decisive factor in determining the HER reaction mechanism of catalysts.[32] Theoretically, the Tafel slope

© 2025 The Author(s). Advanced Materials published by Wiley-VCH GmbH

15214095, 2025, 34, Downloaded from https://advanced.onlinelibrary.wiley.com/doi/10.1002/adma.202419360 by University of Adelaide Alumni, Wiley Online Library on [02/11/2025]. See the Terms and Conditions (https://onlinelibrary.wiley.com/terms-and-conditions) on Wiley Online Library for rules of use; OA articles are governed by the applicable Creative Commons License

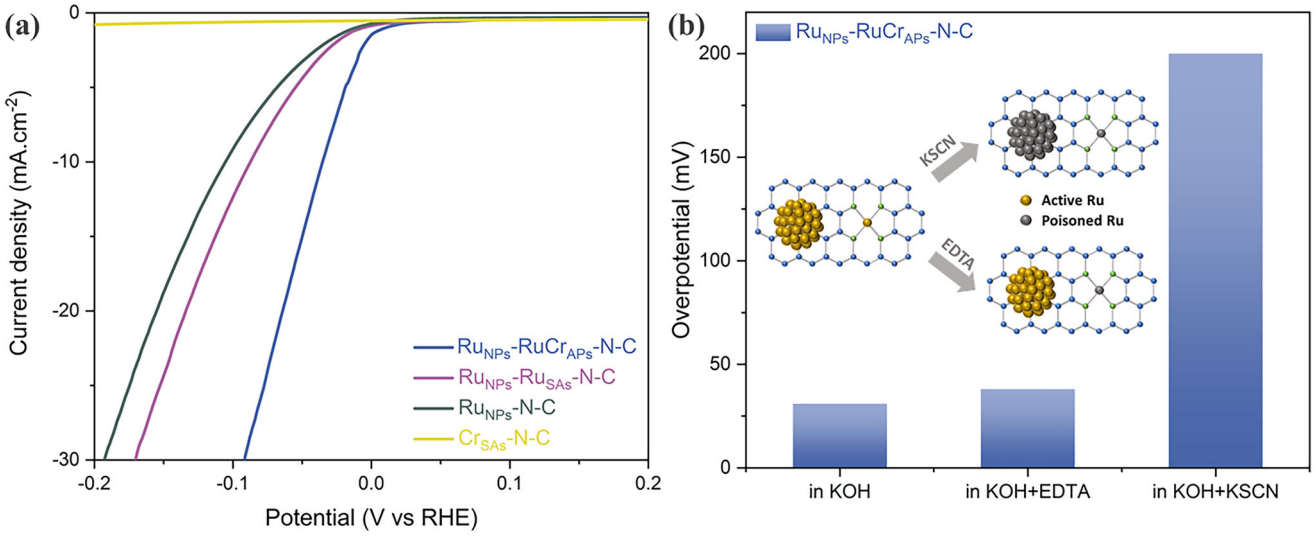

Figure 4. a) Comparison the activity of Ru_{NPs}-$RuCr_{APs}$-N-C, Ru_{NPs}-Ru_{SAs}-N-C, Ru_{NPs}-N-C with Cr_{SAs}-N-C b) Catalyst poisoning experiments of Ru_{NPs}-$RuCr_{APs}$-N-C in 1 M KOH with the addition of 10 mM EDTA and 10 mM KSCN at current density of 10 $mA.cm^{-2}$ (inset: schematic of poisoning experiments).

values are 120 mV dec^{-1} for the Volmer step, 40 mV dec^{-1} for the Heyrovsky step, and 30 mV dec^{-1} for the Tafel step, with each value representing its role as the rate-determining step in the HER.[33] In this work, the Tafel slopes of Ru_{NPs}-Ru_{SAs}-N-C and Ru_{NPs}-$RuCr_{APs}$-N-C electrocatalysts exceed 30 mV dec^{-1} (Figure 3b), suggesting that the HER follows the Volmer-Heyrovsky mechanism where the water adsorption and dissociation are rate determining steps for the HER. Therefore, density functional theory (DFT) calculation was first conducted to understand water adsorption and dissociation ability of Ru SAs, RuCr atomic pairs and RuCr without interaction-modified Ru NPs.

$$\text{Volmer reaction}: \quad H_2O + e^- \rightarrow H^* + OH^- \qquad (\text{Tafelslope} = 120\text{mVdec}^{-1}) \qquad (1)$$

$$\text{Heyrovsky reaction}: \quad H_2O + e^- + H^* \rightarrow H_2 + OH^- \qquad (\text{Tafel slope} = 40\ \text{mV dec}^{-1}) \qquad (2)$$

$$\text{Tafel reaction}: H^* + H^* \rightarrow H_2\ (\text{Tafel slope} = 30\ \text{mV dec}^{-1}) \qquad (3)$$

Different structures of the catalysts including Ru_{NPs}-N-C, Ru_{NPs}-Ru_{SAs}-N-C, Ru_{NPs}-$RuCr_{APs}$-N-C, and Ru_{NPs}-Ru_{SAs}+Cr_{SAs}-N-C (without RuCr atomic interaction) models were proposed (**Figure** 5a–d) based on the structure of the catalyst studied by TEM, XAS and XPS results. As confirmed by the experimental results, Ru NPs serve as the main active sites for HER. Therefore, the Gibbs free energy of water molecule adsorbed on different species modified Ru NPs (ΔG_{W^*}) was calculated and is shown in Figure 5e. It can be seen that both Ru_{NPs}-Ru_{SAs}-N-C (-0.42 eV) and Ru_{NPs}-$RuCr_{APs}$-N-C (-0.41 eV) exhibit obviously reduced ΔG_{W^*} compared to that of Ru_{NPs}-N-C (-0.40 eV), indicating the enhancement of water adsorption ability due to the introduction of Ru SAs and RuCr atomic pairs. In contrast, the water adsorption energy of Ru_{NPs}-Ru_{SAs}+Cr_{SAs}-N-C (-0.35 eV) indicates that this structure is less favorable for water adsorption, highlighting the essential role of Ru SAs and RuCr atomic pairs in modifying EMSI effects and facilitating H_2O adsorption.

The water dissociation ability was evaluated by calculating co-adsorption energy of H* and *OH intermediates (ΔG(H*+*OH)) on different species-modified Ru NPs.[34] As can be seen from Figure 5f, the RuCr atomic pairs modified Ru NPs sites indicate the most negative ΔG(H*+*OH) value (-1.22 eV) among all the structures. This confirms that the RuCr atomic pairs modified Ru NPs sites demonstrate the best water dissociation ability by co-adsorption of H* and *OH intermediates compared to other structures. Therefore, it can be concluded that Ru_{NPs}-$RuCr_{APs}$-N-C catalyst, with $RuCr_{APs}$ modified Ru NPs demonstrates optimised EMSI, which contributes to improved alkaline HER activity by improving the water adsorption ability and reducing energy barrier to dissociate water. Although the calculation results show that there is slight enhancement in the water dissociation ability of Ru_{NPs}-$RuCr_{APs}$-N-C compared to that of other catalysts, the experimental results (Figures 3a–c, Figure 4a; Figure S17b, Supporting Information) strongly confirm the crucial role of atomic pairs in improving the activity of Ru_{NPs}-$RuCr_{APs}$-N-C compared to that of Ru_{NPs}-Ru_{SAs}-N-C and Ru_{NPs}-N-C.

Bader charge analysis was also conducted to understand the charge distribution, which is a critical descriptor in EMSI.[35] The results (Figure S18, Supporting Information) confirm that Ru NPs sites of the catalyst modified by RuCr atomic pairs (Ru_{NPs}-$RuCr_{APs}$-N-C) donate the least electrons to the support, indicating that the Ru NPs of Ru_{NPs}-$RuCr_{APs}$-N-C are the most electron rich compared to the other structures, which is also beneficial for the H_2O dissociation.[25,36]

The Gibbs free energy of hydrogen adsorption (ΔG_{H^*}) was also calculated to evaluate the H_2 desorption ability for all structures

© 2025 The Author(s). Advanced Materials published by Wiley-VCH GmbH

15214095, 2025, 34, Downloaded from https://advanced.onlinelibrary.wiley.com/doi/10.1002/adma.202419360 by University of Adelaide Alumni, Wiley Online Library on [02/11/2025]. See the Terms and Conditions (https://onlinelibrary.wiley.com/terms-and-conditions) on Wiley Online Library for rules of use; OA articles are governed by the applicable Creative Commons License

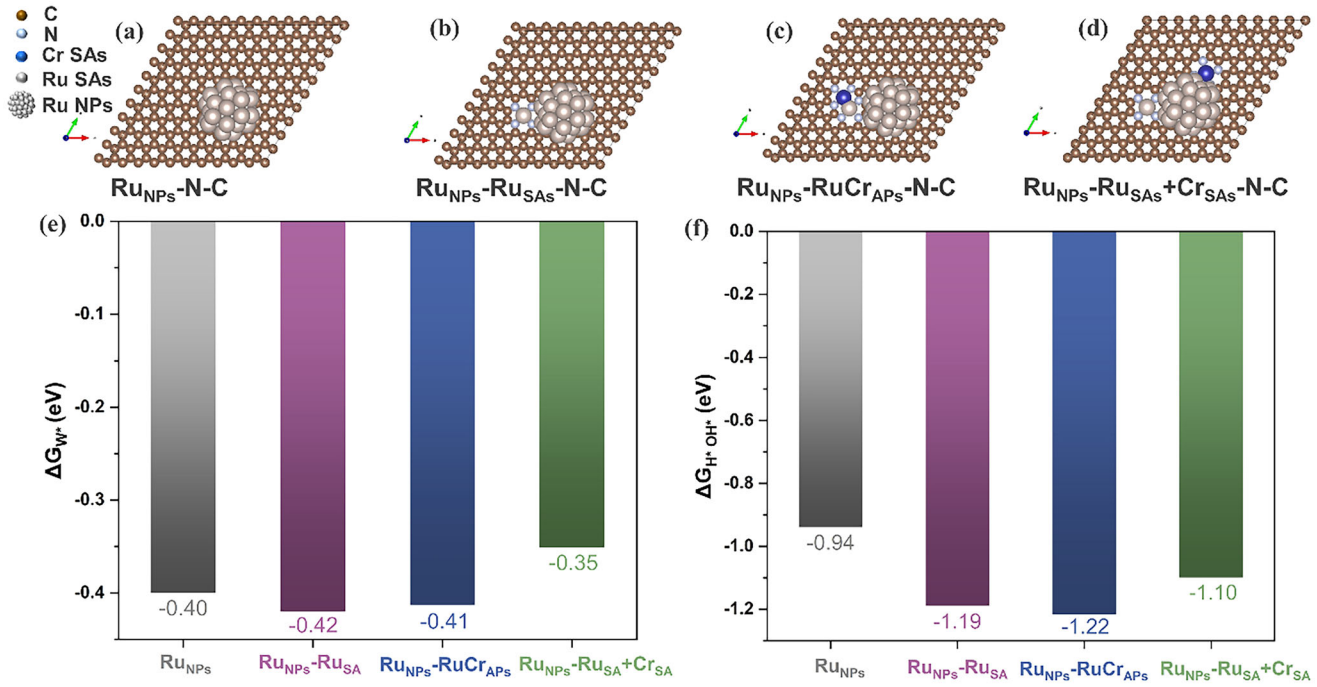

Figure 5. a–d) Proposed model for different structures, e) Water adsorption energies, ΔG(W*), and f) Dissociated water adsorption energies, ΔG(H*+*OH), for different structures of Ru-based catalysts anchored on N-C on Ru NPs site.

on Ru NPs sites. However, the results (Figure S19, Supporting Information) reveal that Ru NPs has strong bond with hydrogen with high obtained ΔG_{H^*}. Therefore, the possibility of hydrogen adsorption on different SAs sites was also evaluated. It is found that H_2 desorption on Ru SAs of Ru_{NPs}-$RuCr_{APs}$-N-C exhibits the least energy barrier among all the structure, which then followed by Cr SAs (Figure S20, Supporting Information). Considering the Gibbs free energy for different reactions and species, the synergistic effect between different active sites is revealed. Ru NPs are the preferred active sites for water molecule's adsorption and dissociation, whereas Ru SAs and Cr SAs of atomic RuCr pairs are the preferred active sites for H_2 desorption.

Combining the experimental results and theoretical calculations, the $RuCr_{APs}$ modified Ru NPs are identified as the active sites for alkaline HER. By improving the water adsorption and dissociation kinetics through optimised EMSI, the Ru_{NPs}-$RuCr_{APs}$-N-C exhibits significantly enhanced performance compared to Ru_{NPs}-Ru_{SAs}-N-C. Additionally, the atomic Ru sites of $RuCr_{APs}$ may contribute to the hydrogen desorption process of the reaction.

3. Conclusion

In summary, we proposed a novel strategy of introducing the $RuCr_{APs}$ into Ru NPs to modify the electronic structure of Ru NPs through the optimized EMSI effects. Ru_{NPs}-$RuCr_{APs}$-N-C catalyst shows promising activity, with the mass activity of 11.33 A·mg^{-1} at an overpotential of 100 mV and a high stability of over 50 h, which is among the highest-performing Ru-based catalysts in alkaline HER reported so far. The experimental results confirmed that the electronically modified Ru NPs are the main active sites for enhanced HER performance. The combination of experimental studies with DFT calculations shows that the critical role of RuCr atomic pairs interaction in the optimization of EMSI effects and facilitation of adsorption and dissociation of water, which is the rate-determining step of alkaline HER. Besides, the binding interaction formed between Ru and Cr atomic pairs also plays a vital role in modifying hydrogen intermediates and promoting the H_2 desorption on the Ru sites. This work offers new perspectives and understandings of developing atomic species-modified electrocatalysts for alkaline HER, while the findings can also benefit the design of other catalysts at the atomic level.

Supporting Information

Supporting Information is available from the Wiley Online Library or from the author.

Acknowledgements

This work was supported by the Australian Research Council (ARC) Training Centre for the Global Hydrogen Economy (IC200100023), ARC Centre of Excellence for Carbon Science and Innovation (CE230100032) and ARC Hub for Integrated Energy Storage Solution (IH180100020). X.L. acknowledges the UNSW Scientia Scheme for financial supports. The authors acknowledge the facilities and the scientific and technical assistance of Microscopy Australia at the Electron Microscope Unit (EMU), and other characterization facilitates within the Mark Wainwright Analytical Centre (MWAC) at UNSW Sydney. This work was undertaken in part using the MEX-1 beamline (AS241/MEX1/21367) and XAS beamline (AS241/XAS/21430) at the Australian Synchrotron, part of ANSTO. The authors also thank Dr. Rosalie Hocking, Dr. Emily Finch, and Dr. Krystina Lamb for their support and assistance with the XAS measurements.

© 2025 The Author(s). Advanced Materials published by Wiley-VCH GmbH

15214095, 2025, 34, Downloaded from https://advanced.onlinelibrary.wiley.com/doi/10.1002/adma.202419360 by University of Adelaide Alumni, Wiley Online Library on [02/11/2025]. See the Terms and Conditions (https://onlinelibrary.wiley.com/terms-and-conditions) on Wiley Online Library for rules of use; OA articles are governed by the applicable Creative Commons License

Open access publishing facilitated by University of New South Wales, as part of the Wiley - University of New South Wales agreement via the Council of Australian University Librarians.

Conflict of Interest

The authors declare no conflict of interest.

Author Contributions

P.E. conceived experiments, conducted data analysis, and wrote the first manuscript. S.Z., X.L., and R.A supervised the project and revised the manuscript. J.Y. helped with DFT calculations and analysis. R.W helped with TEM analysis. D.G. helped with XAS measurements and analysis. Z.M. assisted with EIS data analysis. All authors contributed to the manuscript revision. All authors have given approval to the final version of the manuscript.

Data Availability Statement

The data that support the findings of this study are available from the corresponding author upon reasonable request.

Keywords

alkaline hydrogen evolution reaction, atomic pairs, electronic metal support interaction, ruthenium nanoparticles

Received: December 10, 2024
Revised: March 8, 2025
Published online: March 20, 2025

[1] a) F. Liu, C. Shi, X. Guo, Z. He, L. Pan, Z. F. Huang, X. Zhang, J. J. Zou, *Adv. Sci.* **2022**, *9*, 2200307; b) Y. Luo, Z. Zhang, M. Chhowalla, B. Liu, *Adv. Mater.* **2022**, *34*, 2108133; c) D. Guan, B. Wang, J. Zhang, R. Shi, K. Jiao, L. Li, Y. Wang, B. Xie, Q. Zhang, J. Yu, *Energy Environ. Sci.* **2023**, *16*, 4926.

[2] a) H. Hong, H. Y. Kim, W. I. Cho, H. C. Song, H. C. Ham, K. Chae, F. M. Mota, J. Y. Kim, D. H. Kim, *J. Mater. Chem. A* **2023**, *11*, 5328; b) Z. Y. Yu, Y. Duan, X. Y. Feng, X. Yu, M. R. Gao, S. H. Yu, *Adv. Mater.* **2021**, *33*, 2007100; c) H. G. Xu, X. Y. Zhang, Y. Ding, H. Q. Fu, R. Wang, F. Mao, P. F. Liu, H. G. Yang, *Small Struct.* **2023**, *4*, 2200404.

[3] a) C. Rong, X. Shen, Y. Wang, L. Thomsen, T. Zhao, Y. Li, X. Lu, R. Amal, C. Zhao, *Adv. Mater.* **2022**, *34*, 2110103; b) Y. L. Wu, X. Li, Y. S. Wei, Z. Fu, W. Wei, X. T. Wu, Q. L. Zhu, Q. Xu, *Adv. Mater.* **2021**, *33*, 2006965.

[4] a) L. Peng, D. Zhang, Z. Ma, D. Chu, C. Cazorla, R. Amal, Z. Han, *Small Struct.* **2023**, *4*, 2300194; b) Y. Zuo, S. Bellani, G. Saleh, M. Ferri, D. V. Shinde, M. I. Zappia, J. Buha, R. Brescia, M. Prato, R. Pascazio, *J. Am. Chem. Soc.* **2023**, *145*, 21419; c) Y. Pan, J. Gao, E. Lv, T. Li, H. Xu, L. Sun, A. Nairan, Q. Zhang, *Adv. Funct. Mater.* **2023**, *33*, 2303833; d) J. Zhang, G. Chen, Q. Liu, C. Fan, D. Sun, Y. Tang, H. Sun, X. Feng, *Angew. Chem., Int. Ed.* **2022**, *61*, 202209486.

[5] a) J. Yu, Y. Guo, S. She, S. Miao, M. Ni, W. Zhou, M. Liu, Z. Shao, *Adv. Mater.* **2018**, *30*, 1800047; b) J. Li, Y. Li, J. Wang, C. Zhang, H. Ma, C. Zhu, D. Fan, Z. Guo, M. Xu, Y. Wang, *Adv. Funct. Mater.* **2022**, *32*, 2109439; c) X. Fan, C. Liu, M. Wu, B. Gao, L. Zheng, Y. Zhang, H. Zhang, Q. Gao, X. Cao, Y. Tang, *Appl. Catal., B* **2022**, *318*, 121867.

[6] a) C. H. Chen, D. Wu, Z. Li, R. Zhang, C. G. Kuai, X. R. Zhao, C. K. Dong, S. Z. Qiao, H. Liu, X. W. Du, *Adv. Energy Mater.* **2019**, *9*, 1803913; b) Q. He, Y. Zhou, H. Shou, X. Wang, P. Zhang, W. Xu, S. Qiao, C. Wu, H. Liu, D. Liu, *Adv. Mater.* **2022**, *34*, 2110604.

[7] a) Q. Hu, G. Li, X. Huang, Z. Wang, H. Yang, Q. Zhang, J. Liu, C. He, *J. Mater. Chem. A* **2019**, *7*, 19531; b) J. N. Tiwari, A. M. Harzandi, M. Ha, S. Sultan, C. W. Myung, H. J. Park, D. Y. Kim, P. Thangavel, A. N. Singh, P. Sharma, *Adv. Energy Mater.* **2019**, *9*, 1900931; c) B. Yan, D. Liu, X. Feng, M. Shao, Y. Zhang, *Adv. Funct. Mater.* **2020**, *30*, 2003007; d) T. Luo, J. Huang, Y. Hu, C. Yuan, J. Chen, L. Cao, K. Kajiyoshi, Y. Liu, Y. Zhao, Z. Li, *Adv. Funct. Mater.* **2023**, *33*, 2213058.

[8] C. Hu, E. Song, M. Wang, W. Chen, F. Huang, Z. Feng, J. Liu, J. Wang, *Adv. Sci.* **2021**, *8*, 2001881.

[9] S. Wang, M. Wang, Z. Liu, S. Liu, Y. Chen, M. Li, H. Zhang, Q. Wu, J. Guo, X. Feng, *ACS Appl. Mater. Interfaces* **2022**, *14*, 15250.

[10] H. Yao, X. Wang, K. Li, C. Li, C. Zhang, J. Zhou, Z. Cao, H. Wang, M. Gu, M. Huang, *Appl. Catal., B* **2022**, *312*, 121378.

[11] a) L. Cai, H. Bai, C. w. Kao, K. Jiang, H. Pan, Y. R. Lu, Y. Tan, *Small* **2024**, *20*, 2311178; b) R. Liu, M. Sun, X. Liu, Z. Lv, X. Yu, J. Wang, Y. Liu, L. Li, X. Feng, W. Yang, *Angew. Chem., Int. Ed.* **2023**, *62*, 202312644.

[12] a) M. Xiao, Y. Chen, J. Zhu, H. Zhang, X. Zhao, L. Gao, X. Wang, J. Zhao, J. Ge, Z. Jiang, *J. Am. Chem. Soc.* **2019**, *141*, 17763; b) S. Ji, Y. Chen, Q. Fu, Y. Chen, J. Dong, W. Chen, Z. Li, Y. Wang, L. Gu, W. He, *J. Am. Chem. Soc.* **2017**, *139*, 9795.

[13] M. Liu, H. Chun, T.-C. Yang, S. J. Hong, C.-M. Yang, B. Han, L. Y. S. Lee, *ACS Nano* **2022**, *16*, 10657.

[14] a) X. Hu, G. Luo, Q. Zhao, D. Wu, T. Yang, J. Wen, R. Wang, C. Xu, N. Hu, *J. Am. Chem. Soc.* **2020**, *142*, 16776; b) Y. Ma, H. Qu, Z. Chi, X. Liu, Y. Yu, Z. Guo, L. Wang, *Nano Res.* **2022**, *15*, 3204.

[15] a) D. Li, Y. Liu, Z. Liu, J. Yang, C. Hu, L. Feng, *J. Mater. Chem. A* **2021**, *9*, 15019; b) T. Li, J. Yin, D. Sun, M. Zhang, H. Pang, L. Xu, Y. Zhang, J. Yang, Y. Tang, J. Xue, *Small* **2022**, *18*, 2106592.

[16] J. Zhu, S. Mu, *Adv. Funct. Mater.* **2020**, *30*, 2001097.

[17] a) D. Meng, J. Zheng, J. Guo, A. Zhang, Z. Wang, *Small* **2025**, *21*, 2408146; b) X. Li, Y. Y. Liu, C. Li, H. Xue, S. Chen, Q. Xu, H. Pang, *Adv. Sci.* **2024**, *11*, 2310181.

[18] a) X. Huo, J. Huang, M. Gao, W. Zhu, W. Liu, Q. Liu, L. Cao, K. Kajiyoshi, Y. Zhao, Y. Liu, *ACS Appl. Energy Mater.* **2024**, *7*, 2862; b) S. Ji, Y. Chen, S. Zhao, W. Chen, L. Shi, Y. Wang, J. Dong, Z. Li, F. Li, C. Chen, *Angew. Chem., Int. Ed.* **2019**, *58*, 4271.

[19] Y. Li, L. A. Zhang, Y. Qin, F. Chu, Y. Kong, Y. Tao, Y. Li, Y. Bu, D. Ding, M. Liu, *ACS Catal.* **2018**, *8*, 5714.

[20] G. M. Tomboc, T. Kim, S. Jung, H. J. Yoon, K. Lee, *Small* **2022**, *18*, 2105680.

[21] K. Sato, S. Zaitsu, G. Kitayama, S. Yagi, Y. Kayada, Y. Nishida, Y. Wada, K. Nagaoka, *JACS Au* **2022**, *2*, 1627.

[22] P. Su, W. Pei, X. Wang, Y. Ma, Q. Jiang, J. Liang, S. Zhou, J. Zhao, J. Liu, G. Q. Lu, *Angew. Chem., Int. Ed.* **2021**, *60*, 16044.

[23] H. Qi, J. Yang, F. Liu, L. Zhang, J. Yang, X. Liu, L. Li, Y. Su, Y. Liu, R. Hao, *Nat. Commun.* **2021**, *12*, 3295.

[24] A. A. Adeniyi, P. A. Ajibade, *J. Chem.* **2016**, *2016*, 3672062.

[25] S. Wang, X. Ning, X. Liu, M. Shakouri, Y. Hu, H. Yuan, P. Liu, X. Lu, Y. Guo, Y. Wang, *Carbon* **2024**, *217*, 118611.

[26] Y. Bai, H. Zhang, X. Lu, L. Wang, Y. Zou, J. Miao, M. Qiao, Y. Tang, D. Zhu, *Chem.-Eur. J.* **2023**, *29*, e202300205.

[27] C. Tsounis, B. Subhash, P. V. Kumar, N. M. Bedford, Y. Zhao, J. Shenoy, Z. Ma, D. Zhang, C. Y. Toe, S. Cheong, *Adv. Funct. Mater.* **2022**, *32*, 2203067.

[28] L. Korampattu, S. Barik, A. Pandikassala, R. R. Urkude, S. Kurungot, P. L. Dhepe, *Chem. Mater.* **2024**, *36*, 4262.

[29] a) B. Zheng, L. Ma, B. Li, D. Chen, X. Li, J. He, J. Xie, M. Robert, T.-C. Lau, *Catal. Sci. Technol.* **2020**, *10*, 4405; b) J. Mahmood, F. Li, S.-M. Jung, M. S. Okyay, I. Ahmad, S.-J. Kim, N. Park, H. Y. Jeong, J.-B. Baek, *Nat. Nanotechnol.* **2017**, *12*, 441; c) C.-B. Hong, X. Li, W.-B. Wei, X.-T. Wu, Q.-L. Zhu, *Appl. Catal., B* **2021**, *294*, 120230;

© 2025 The Author(s). Advanced Materials published by Wiley-VCH GmbH

15214095, 2025, 34, Downloaded from https://advanced.onlinelibrary.wiley.com/doi/10.1002/adma.202419360 by University of Adelaide Alumni, Wiley Online Library on [02/11/2025]. See the Terms and Conditions (https://onlinelibrary.wiley.com/terms-and-conditions) on Wiley Online Library for rules of use; OA articles are governed by the applicable Creative Commons License

d) H. Wang, C. Xu, Q. Chen, M. Ming, Y. Wang, T. Sun, Y. Zhang, D. Gao, J. Bi, G. Fan, *ACS Sustainable Chem. Eng.* **2018**, *7*, 1178; e) C. Wang, P. Li, L. Zong, K. Fan, F. Lu, Z. Wang, L. Wang, *J. Alloys Compd.* **2023**, *967*, 171667; f) L.-N. Chen, S.-H. Wang, P.-Y. Zhang, Z.-X. Chen, X. Lin, H.-J. Yang, T. Sheng, W.-F. Lin, N. Tian, S.-G. Sun, *Nano Energy* **2021**, *88*, 106211; g) J. Chen, J. Huang, Y. Zhao, L. Cao, K. Kajiyoshi, Y. Liu, Z. Li, Y. Feng, *Chem. Eng. J.* **2022**, *450*, 138026; h) Y. Li, H. Liu, B. Li, Z. Yang, Z. Guo, J.-B. He, J. Xie, T.-C. Lau, *J. Mater. Chem. A* **2021**, *9*, 12196; i) Y. Feng, W. Feng, J. Wan, J. Chen, H. Wang, S. Li, T. Luo, Y. Hu, C. Yuan, L. Cao, *Appl. Catal., B* **2022**, *307*, 121193; j) Z. Xu, M. Fan, S. Tan, R. Wang, W. Tu, X. Huang, H. Pan, H. Zhang, H. Tang, *J. Colloid Interface Sci.* **2024**, *657*, 870; k) Y. Liu, X. Li, Q. Zhang, W. Li, Y. Xie, H. Liu, L. Shang, Z. Liu, Z. Chen, L. Gu, *Angew. Chem., Int. Ed.* **2020**, *59*, 1718; l) J. Zhang, Y. Gu, Y. Lu, C. Zhu, G. Liu, C. Wang, D. Sun, Y. Tang, H. Sun, *Appl. Catal., B* **2023**, *325*, 122316; m) H. Sun, C.-W. Tung, Y. Qiu, W. Zhang, Q. Wang, Z. Li, J. Tang, H.-C. Chen, C. Wang, H. M. Chen, *J. Am. Chem. Soc.* **2021**, *144*, 1174; n) P. Zhai, M. Xia, Y. Wu, G. Zhang, J. Gao, B. Zhang, S. Cao, Y. Zhang, Z. Li, Z. Fan, *Nat. Commun.* **2021**, *12*, 4587; o) J.-T. Ren, L. Chen, H.-Y. Wang, W.-W. Tian, X. Zhang, T.-Y. Ma, Z. Zhou, Z.-Y. Yuan, *Appl. Catal., B* **2023**, *327*, 122466.

[30] B. Lu, L. Guo, F. Wu, Y. Peng, J. E. Lu, T. J. Smart, N. Wang, Y. Z. Finfrock, D. Morris, P. Zhang, *Nat. Commun.* **2019**, *10*, 631.

[31] a) A. Y. Faid, S. Sunde, *Energy Technol.* **2022**, *10*, 2200506; b) A. P. Murthy, J. Theerthagiri, J. Madhavan, *J. Phys. Chem. C.* **2018**, *122*, 23943.

[32] C. Wan, Y. Ling, S. Wang, H. Pu, Y. Huang, X. Duan, *ACS Cent. Sci.* **2024**, *10*, 658.

[33] a) M.-R. Gao, J.-X. Liang, Y.-R. Zheng, Y.-F. Xu, J. Jiang, Q. Gao, J. Li, S.-H. Yu, *Nat. Commun.* **2015**, *6*, 5982; b) J. Zhu, L. Hu, P. Zhao, L. Y. S. Lee, K.-Y. Wong, *Chem. Rev.* **2019**, *120*, 851.

[34] P. Kuang, Z. Ni, B. Zhu, Y. Lin, J. Yu, *Adv. Mater.* **2023**, *35*, 2303030.

[35] Y. Liu, Q. Wang, J. Zhang, J. Ding, Y. Cheng, T. Wang, J. Li, F. Hu, H. B. Yang, B. Liu, *Adv. Energy Mater.* **2022**, *12*, 2200928.

[36] Q. He, D. Tian, H. Jiang, D. Cao, S. Wei, D. Liu, P. Song, Y. Lin, L. Song, *Adv. Mater.* **2020**, *32*, 1906972.

© 2025 The Author(s). Advanced Materials published by Wiley-VCH GmbH

15214095, 2025, 34, Downloaded from https://advanced.onlinelibrary.wiley.com/doi/10.1002/adma.202419360 by University of Adelaide Alumni, Wiley Online Library on [02/11/2025]. See the Terms and Conditions (https://onlinelibrary.wiley.com/terms-and-conditions) on Wiley Online Library for rules of use; OA articles are governed by the applicable Creative Commons License